ARTICLE

OPEN

Check for updates

Complex strike-slip faulting during the 2021 M$_w$7.4 Maduo earthquake

Guoguang Wei [1], Kejie Chen [1✉], Mingzhe Lyu[1], Wenzheng Gong[1], Luca Dal Zilio[2], Lingling Ye[1] & Hongwei Tu[3]

Fault geometry is an essential component for understanding earthquake genesis and dynamic rupture propagation. Here we employed space-based geodetic observations and geological survey, adopting a fully Bayesian approach, to probabilistically estimate the fault geometry of the 2021 M$_w$7.4 Maduo earthquake. The fault is predominantly characterized by strike-slip motions with three main geometry irregularities, reflecting the segmented pattern of the earthquake rupture. On the west side of the epicenter, the fault exhibits north-dipping angles (75–81°), whereas on the east side, it shows sub-vertical angles (82–87°). For the southeast branch, geodetic inversion reveals an overall shallow-dipping (44 ± 5°) faulting, yet further segmentation of the branch in the model and analysis of aftershock mechnism indicate that the dip of the branch faults may vary between vertical and shallow angles. This finding warrants confirmation through future underground observation data.These results suggest that strike-slip faulting could occur on unsuitably orientated planes during any seismic event.

[1] Department of Earth and Space Sciences, Southern University of Science and Technology, Shenzhen, China. [2] Institute of Geophysics, Department of Earth Sciences, ETH Zürich, Zürich, Switzerland. [3] Qinghai Earthquake Agency, Xining, China. ✉email: chenkj@sustech.edu.cn

Large strike-slip earthquakes usually involve a complex fault geometry with multi-segment faults and variable strike and dip over the entire rupture zone, e.g., the 2001 M_w 7.8 Kunlun[1] and the 2010 M_w 7.2 El Mayor-Cucapah[2] earthquakes. Fault geometry provides vital information for a better understanding of earthquake nucleation and rupture propagation[3]. While changes in strike directions can now be mapped from surface rupture zones measured by geological survey or space-geodetic observations, the variations in the dip angles at depth are still difficult to depict precisely. To this end, much effort has been put in estimating the fault dip at depth. For instance, structural geology[4] and seismic tomography[5] have been developed to probe the underground fault dip. Furthermore, the seismic moment tensor inversion for the mainshock[6] or the aftershock[7] has become an important approach to learning the fault dip at depth. In addition, aftershock locations have also been used to constrain the fault dip at depth[8]. Nevertheless, aftershocks are not always detected and sufficient to determine the fault dip of large strike-slip earthquakes, e.g., the 2013 M_w 7.7 Balochistan earthquake[9]. Owing to the advent of satellite observations, space geodesy has been advanced in the spatial resolution and accuracy that can well model surface ground displacements[10]. Moreover, near-field surface displacements measured by geodetic techniques are sensitive to the faulting processes and can help to resolve the irregularities of the fault geometry[11].

The May 21, 2021 M_w 7.4 Maduo earthquake occurred on the northeast section of the Bayan Har block, one of the most active blocks embedded in the Tibetan Plateau (Fig. 1a). Changes in the strike directions have been measured by space-geodetic observations[12] and geological field survey[13], and it has been indicated that the fault system has a ~150-km-long sinistral strike-slip shear zone with a small branch at the eastmost section. Irregular fault dips at depth have previously been inferred from the aftershock locations[14–17], which commonly indicate sub-vertical fault segments. However, in these studies, the estimation of the fault dip with aftershock locations lacks constraint from high-resolution surface rupture traces, and thus cannot fully characterize the fault dip. For instance, on the southeast section of the fault, the spatial distribution of the aftershocks does not coincide with the surface rupture trace of the geological survey (Fig. 1b).

The fault dip has also been estimated with ground displacements measured by geodetic techniques[18–21]. The estimation of the fault geometry simultaneously with the fault slip from geodetic observations is a nonlinear inversion problem. To seek the optimal fault dip angles that best fit the geodetic observations, previous studies have commonly adopted search-based approaches such as a genetic algorithm[21] or grid search[18–20,22–24]. However, the direct search methods are subject to the setting of the search step and range. Moreover, for the inversion problem of
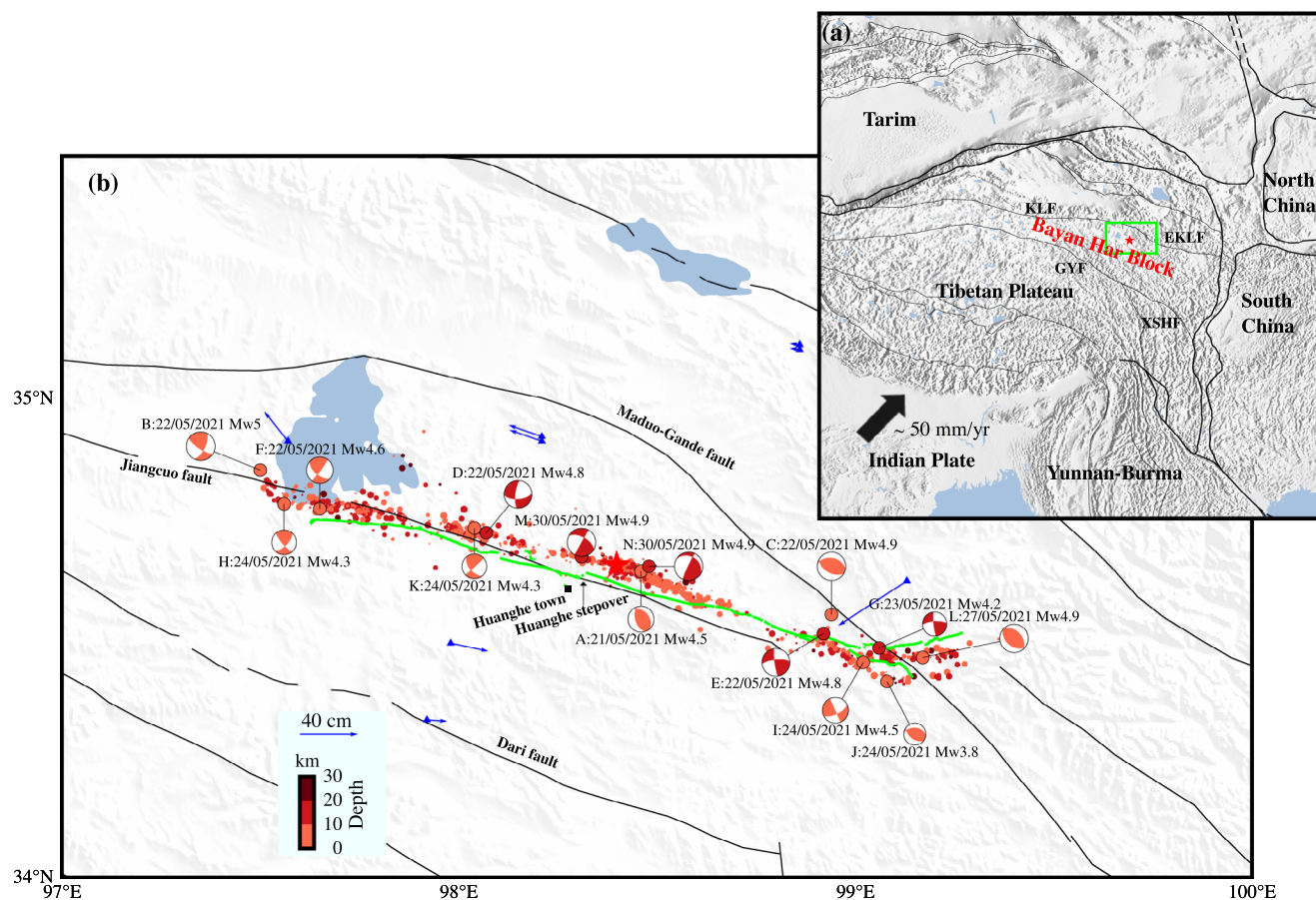

Fig. 1 Tectonic setting. a Tectonic setting of the 2021 M_w 7.4 Maduo earthquake, the epicenter of which is marked by the red star. The solid black traces are the major active tectonic block boundaries[60]. KLF Kunlun fault, EKLF East Kunlun fault, GYF Ganzi–Yushu fault, XSHF Xianshuihe faut. **b** The area marked by the green box in **a**. The blue triangles are GNSS stations, co-seismic horizontal displacements of which are shown with blue arrows[36]. The green line shows the surface rupture trace of the 2021 M_w 7.4 Maduo earthquake, as measured by geological survey[13]. The aftershock sequence 9 days after the mainshock with focal mechanism solutions (beach balls) of $M_w \geq 4$ aftershocks (identified with the occurrence times of events A–I and K–N) is indicated with dots color-coded with depth[16]. The focal mechanism solution of the M_w 3.8 aftershock (event J) estimated in this study is also indicated. The black traces are active faults[61].
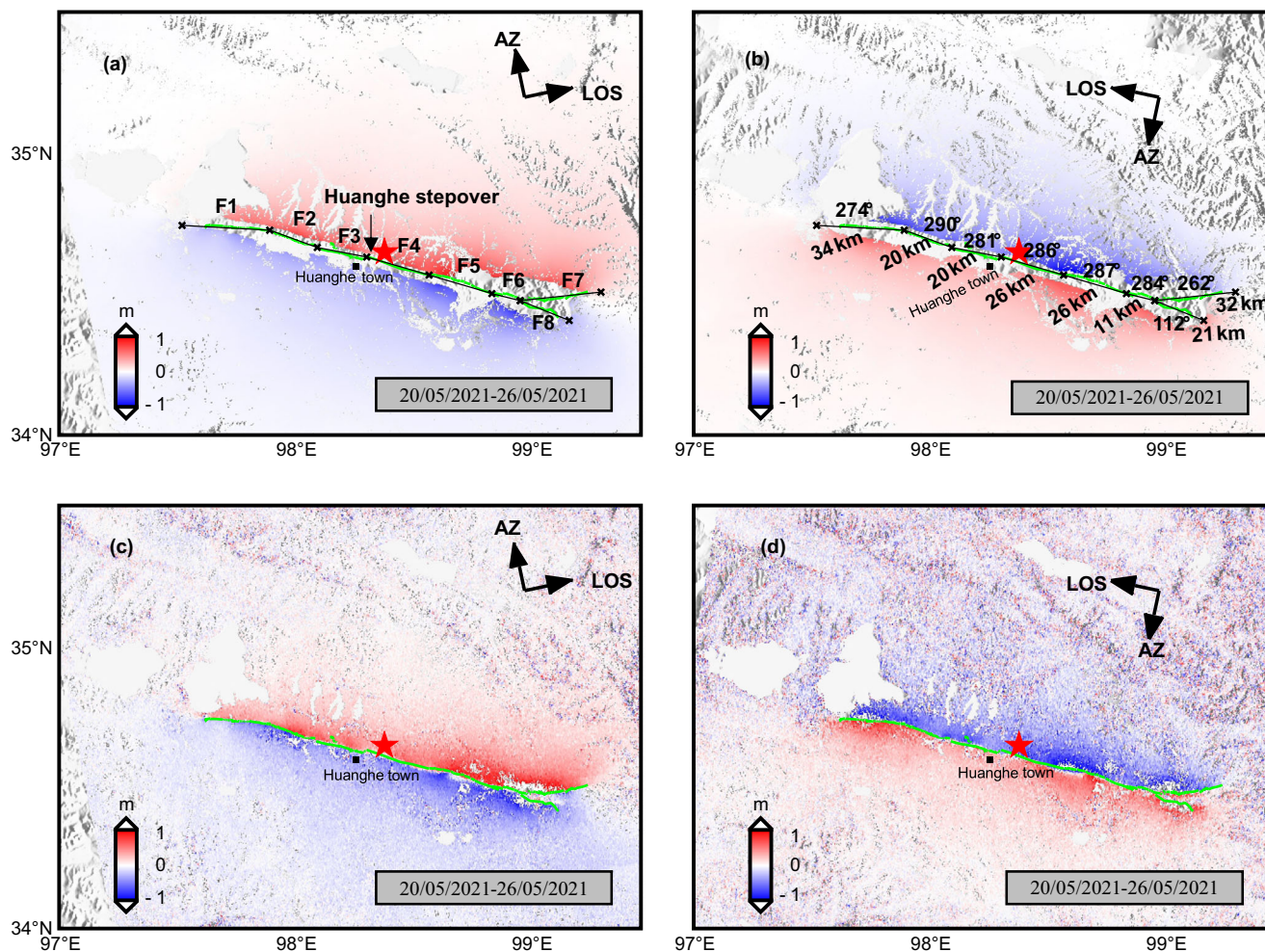
Fig. 2 Coseismic deformation associated with the 2021 Maduo earthquake. a Sentinel-1 LOS displacement (positive towards satellite) map of the ascending track. The green lines show the surface rupture traces measured by geological survey[13], in which a ~2 km-wide releasing step-over near Huanghe town (black square) is marked. F1 to F8 are the eight schematic fault segments discretized based on fault step-overs or bends. **b** Sentinel-1 LOS displacement map of the descending track. The strike angle and length (along-strike direction) for each fault segment are labeled nearby. **c** Sentinel-1 range offset map of the ascending track. **d** Sentinel-1 range offset map of the descending track. AZ azimuthal direction, LOS line of sight.

an earthquake source, there are trade-offs between the model parameters, and it is common that broad values of model parameters can approximately explain the same observations. Therefore, the direct search methods may not fully determine the most plausible estimates or adequately evaluate the uncertainties associated with the estimates. For the complex fault system of the Maduo earthquake, such a problem increases the risk of the parameter estimates being inadequately interpreted. In fact, the fault dip angles estimated in the different studies are actually not in agreement. In particular, it has been reported that the dip of the southeast branch fault shows variable north-dipping or south-dipping angles being between 64° and 90° (Supplementary Table S1).

In contrast, a Bayesian inference method can estimate the probability distributions of the model parameters, and can provide an ensemble of plausible model parameters, with the uncertainties on all the estimates[25–30]. The Bayesian inference method has the advantage of being able to solve nonlinear problems and derive probabilistic estimates. Such probabilistic estimates allow to fully explore possible parameter spaces. Furthermore, it makes it possible to simultaneously invert for the fault geometry and the fault slip from geodetic data[31–33]. For example, the fault geometry of the Maduo earthquake is estimated with Geodetic Bayesian Inversion Software (GBIS)[34,35]. However,

they used a single-segment fault model and inferred an overall 80° north-dipping angle, which does not characterize the irregularities of the fault geometry. In this study, to better resolve the irregularities of the fault geometry—especially on the east section —and to provide new insight into the understanding of the stress environment and rupture propagation, we derived a fully Bayesian inference framework based on multiple geodetic datasets to infer a probabilistic estimate of the fault geometry along the coseismic surface rupture trace obtained from geological survey, and further conducted point-source inversion for the M_w 3.8 aftershock on the southeast branch fault, which can validate the geodetic estimate.

Results

Fault geometry and slip components. Sentinel-1 synthetic aperture radar (SAR) images (Supplementary Table S2) were collected and processed (see Methods) to investigate the coseismic surface deformation maps for the 2021 Maduo earthquake (Fig. 2). We also adopted the coseismic global navigation satellite system (GNSS) displacements[36] (Fig. 1b). The geological survey has been conducted[13] and depicted the high-resolution surface rupture traces (Fig. 1b). We used eight segments along the surface rupture traces to interpret the fault system (Fig. 2a). We treated

each fault segment as a plane with uniform slip. The SAR maps and GNSS measurements were used to estimate probability distributions of dip, width (along the down-dip direction) and slip parameters for each fault plane in a fully Bayesian inference frame (see Methods).

The probability distribution samples of all the model parameters were estimated (Supplementary Figs. S6–S10). As segment F7 and segment F8 are close to each other (Fig. 2a), we first evaluated the trade-offs between their faulting parameter samples (Fig. 3a). Our results indicate that a notable trade-off is found between the strike-slip and the dip angle of segment F8. The strike-slip positively relates to the dip angle. We quantified confidence intervals of the parameters with standard deviations of the parameter samples. Despite the trade-off, the strike-slip and dip angle estimates are still restricted to a small parameter space (Fig. 3b), in which the strike-slip is within 0.92–1.08 m and the dip angle is between 39° and 49°. For the other parameter estimates of segments F7 and F8, there are no obvious positive or negative trade-offs. This illustrates that the geodetic observations used in this study provide good constraints on segments F7 and F8. Further comparisons between the dip angles, width, strike-slip, and dip-slip between the eight segments, as well as the hyperparameters, indicate minor trade-offs between these parameter estimates (Supplementary Figs. S11–S15).

The estimates of the model parameters and the corresponding standard deviations are evaluated by their sample distributions (Fig. 3c). Generally speaking, for the eight fault segments, the irregularities in the fault dip have three main parts identified. Firstly, fault segments F1 to F3 on the west side of the Huanghe step-over (near the epicenter, Fig. 2a) are respectively dipping at $75 \pm 1°$, $81 \pm 1°$, and $75 \pm 2°$ to the north. On these three fault segments, the strike-slip magnitudes are between 1.7 ± 0.08 m and 2.6 ± 0.08 m, which are clearly greater than the dip-slip values of between -0.1 ± 0.03 m and 0.6 ± 0.04 m. In contrast, fault segments F4–F7 on the east side of the Huanghe step-over dip more steeply, and their dip angles are between $82 \pm 1°$ and $87 \pm 1°$. The four fault segments have nearly pure strike-slip motions, in that the dip-slip is almost zero on segment F5. In particular, fault segment F8 shallowly dips $44 \pm 5°$ to the south, and it exhibits the most distinctive geometry, compared to the other fault segments. Despite the small dip angle, fault segment F8 is dominated by the strike-slip component of 1.0 ± 0.08 m coupled with the up-dip component of 0.2 ± 0.08 m. The estimated geometry and slip amplitude of the eight fault segments are shown in Fig. 4a, b.

Due to the relatively small slip amplitude on segment F8, the estimation of the dip angle for F8 could be trapped in a local minimum. To further demonstrate the robustness of the estimation of the dip angle parameter for segment F8, we conducted two additional types of inversions. The first type of inversion involved excluding segment F8 and solely inverting the faulting parameters of the remaining seven segments. The second type of inversion entailed fixing the dip angle of segment F8 at 90° and subsequently inverting the fault parameters of all eight segments. A comparison between three types of inversions reveals that removing F8 or fixing F8 at 90° results in changes in dip angle estimates of the neighboring fault segments F6 and F7 (Supplementary Table S4). Considering the goodness of data fit surrounding segment F8 for three inversion methods (Supplementary Figs. S16–S18), it is evident that the inversion treating the dip angle of segment F8 as the parameter to estimate exhibits the most favorable data fitting (Supplementary Table S5). For the inversion with fixing the dip angle of segment F8 to be vertical, it leads to a decrease in the goodness of fitting to the interferometric and pixel offset data on the descending orbit by 1–3%, while there is no change in the goodness of fitting to the data on the ascending orbit.

This variation in data fitting constitutes a minor percentage. It should be noted that the goodness of fitting to the observational data inevitably encounters challenges arising from data noise. Given the pixel offset data with relatively large noise, the estimation of the dip angle for segment F8, require additional validation through future underground observational data. Finally, the removal of segment F8 leads to a notable decrease in the goodness of data fitting for all data, regardless of whether they are from ascending or descending orbits, with a maximum reduction of 8%. The observed variation in data fit underscores the indispensability and, consequently, the value of segment F8 in comprehending the fault system.

Aftershock sequence and distributed fault slip model. Although pure strike-slip motion is expected on a subvertical fault, our geodetic estimate of the southeast branch fault (segment F8) indicates that the strike-slip component (1.0 m) is significantly greater than the dip-slip component (0.2 m). The segment denotes another rare example of dominant strike-slip motion on a shallow-dipping fault with the $44 \pm 5°$ dip angle, as in, for example, the strike-slip faulting with the 45° dip angle during the 2013 M_w 7.7 Balochistan earthquake[9]. The 2021 M_w 7.4 Maduo earthquake was followed by 13 $M_w \geq 4$ aftershocks (events A–I and K–N identified with the occurrence time in Fig. 1b and Supplementary Table S6)[16]. Such moderate to strong aftershocks can help us to interpret the fault geometry of the southeast branch fault. Among the moderate to strong aftershocks, the aftershock closest to the southeast branch fault (segment F8) is event I (Fig. 4a, b). However, the perpendicular distance from the centroid location of event I to the southeast branch fault surface is 3.7 km (Fig. 4d).

To better interpret the southeast branch fault (segment F8), we carefully checked the aftershock sequence on the south side of the southeast branch fault based on the aftershock catalog[14]. We found that the second-largest magnitude 3.8 aftershock occurred after the M_w 4.5 aftershock (event I). The aftershock occurred on May 24, 2021, and is assigned as identifier J (Fig. 1b). We performed a point-source inversion for event J by the Cut-And-Paste (CAP) method[37–40] with the local seismic velocity model[14,41,42] (Supplementary Fig. S19) using the regional broadband recordings from 25 stations mostly within 300 km of the epicenter (see Supplementary Fig. S20a). In the inversion, we estimate the seismic moment and strike, dip, and rake of a nodal plane, and conduct a grid search for the optimal depth from 3.0 km to 9.5 km with an interval of 0.5 km. The optimal centroid depth is at 5.5 km (Supplementary Fig. S20b). The centroid location of event J at the optimal depth has only the 0.1 km perpendicular distance to the southeast branch fault surface (Fig. 4d). The inversion at the optimal depth has a best double-couple solution for one nodal plane with strike $\phi_1 = 276°$, dip $\delta_1 = 42°$, and rake $\lambda_1 = 64°$, and a second nodal plane with strike $\phi_2 = 129°$, dip $\delta_2 = 53°$, and rake $\lambda_2 = 112°$. The inverted seismic moment M_0 is 6.281×10^{14} N·m (M_w 3.8). Considering the geometry of segment F8 (strike = 112°, dip = $44 \pm 5°$, Fig. 4a), the second nodal plane of the M_w 3.8 aftershock (event J) with strike $\phi_2 = 129°$ and dip $\delta_2 = 53°$ toward the south direction therefore appears to support the geodetic estimate of segment F8, implying the existence of a shallow-dipping fault.

Our estimation of the dip angle for segment F8 has indicated the presence of an overall shallow-dipping fault plane. As demonstrated by aftershock event I that has nodal plane I (strike = 65°, dip = 65°) and nodal plane II (strike = 156°, dip = 88°) (Supplementary Table S6), F8 may also contain a steeper sub-fault. Based on the locations of aftershock events I and J, we divided F8 into two segments (F8a and F8b), resulting
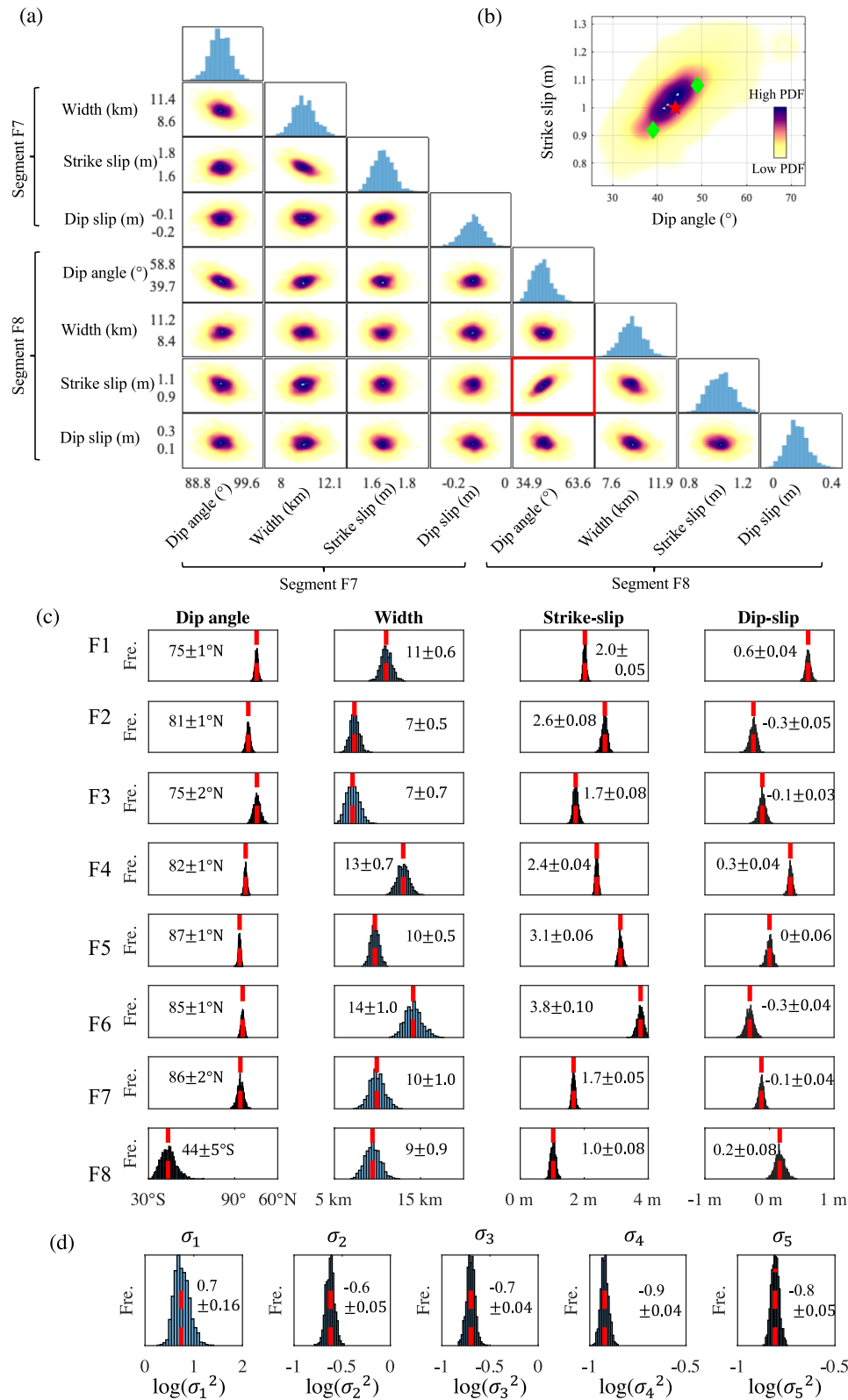
Fig. 3 Posterior samples of the faulting parameters based on the Bayesian inference. a 2D probability density functions (PDFs) between the faulting parameters of segments F7 and F8. A dip angle larger than 90° means a north-dipping angle, the real angle is equal to 180° minus the angle value. The red box outlines the 2D PDF between the strike slip and the dip angle of segment F8, as shown in **b**. The red star denotes the median of the posterior samples for the dip angle and the strike slip. Confidence intervals of the parameters are evaluated by standard deviations of the posterior parameter samples, and the two green diamonds respectively show the possible maximum and minimum locations of the dip angle and the strike slip. **c** Posterior samples of the dip angles, width, strike slips, and dip slips. **d** Posterior samples of the five hyperparameters. The median and standard deviation of posterior samples on each panel are annotated nearby. For the dip angle parameter, S represents the south-dipping angle and N denotes the north-dipping angle. The positive value for dip-slip denotes the up-dip direction. The dashed red line marks the median of the samples for each parameter.
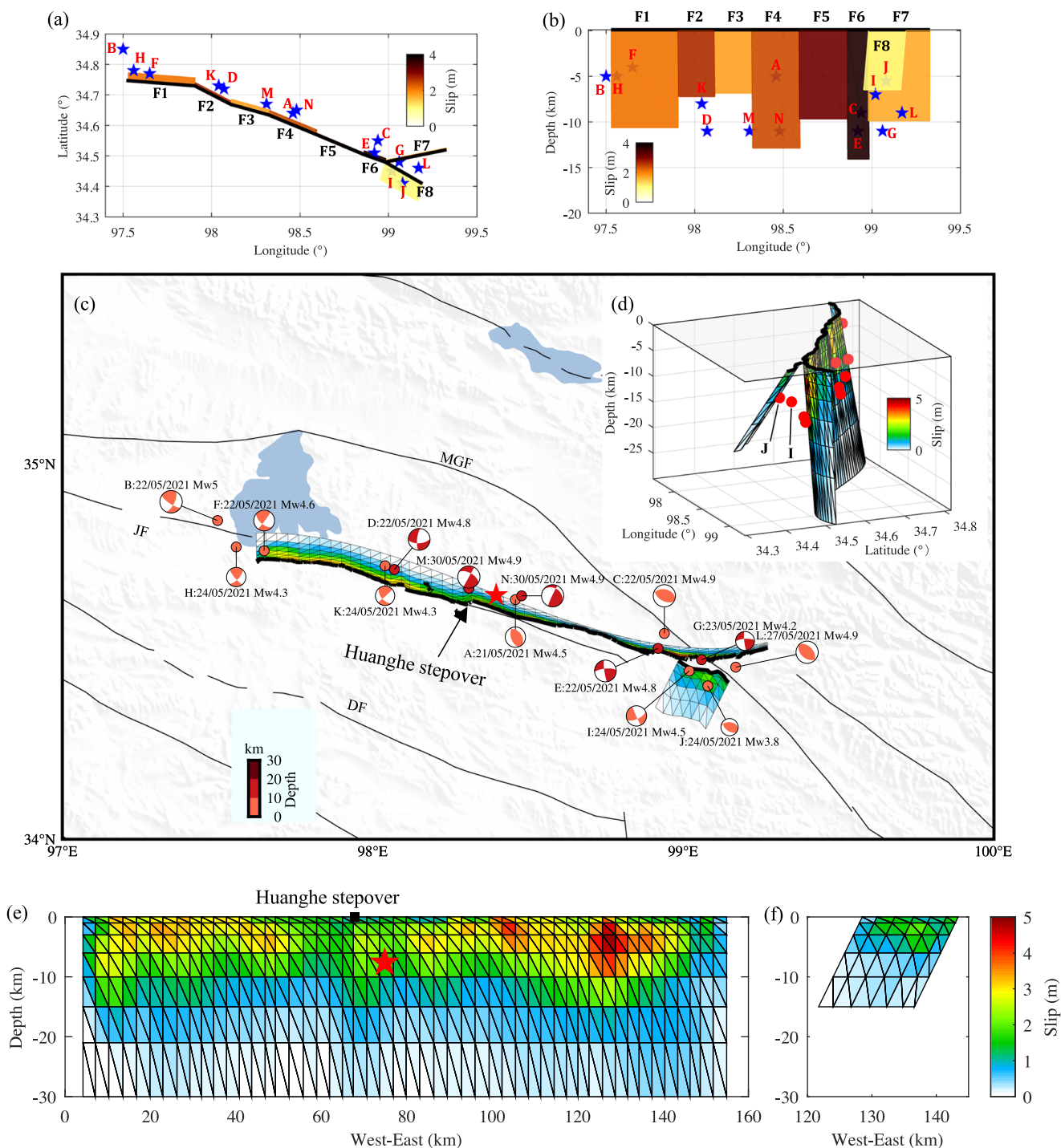
Fig. 4 Fault geometry and slip. a Top view and **b** front view (from south to north) of the geometry and slip for the eight fault planes estimated with the sample medians. The blue stars mark the locations of aftershock events A–N, which are labeled by the beach balls color-coded with depth in **c** the tectonic setting with the distributed fault slip model, **d** the 3-D view of which is also indicated. Perpendicular distances from the centroid location of events I and J to the fault surface of the southeast branch are 3.7 km and 0.1 km, respectively. The front view (from south to north) of the fault slip distribution on **e** the main fault and **f** the southeast branch fault is also indicated. MGF Maduo-Gande fault, JF Jiangcuo fault, DF Dari fault.

in nine fault segments (Supplementary Fig. S21). The inversion for the nine-segment geometry indicate that the dip angle estimates of segments F8a and F8b converge at a north-dipping angle of 71 ± 4°, and a south-dipping angle of 25 ± 3°, respectively (Supplementary Fig. S22). Based on this fault geometry, the perpendicular distance from the centroid location of event I to fault plane F8a is 3.4 km, and the perpendicular distance from the centroid location of event J to fault plane F8b is 3.3 km

(Supplementary Fig. S23). From this perspective, events I and J do not exhibit discernible correlation with the double-segment fault model. The results indicate that the two aftershocks are insufficient to draw a robust conclusion regarding whether segment F8 is vertical or shallow-dipping. Both the existence of a shallow-dipping segment and a vertical segment are equally probable. On the other hand, the inclusion of two segments, namely F8a and F8b, introduces complexity in the model

parameters. F8a may necessitate a greater length, whereas F8b may require a shorter length. This presents numerous potential combinations, making it challenging to determine the most suitable arrangement given the application of the geodetic data implemented in this particular investigation. The primary aim of this study is to ascertain the overall faulting pattern observed in segment F8, encompassing the amalgamated impact of F8a and F8b. Our contention is that by discerning the overarching faulting trend of segment F8, we can acquire fundamental insights into the structural deformation and seismogenic mechanism underlying the 2021 M_w7.4 Maduo event.

To further understand the interplay between the fault geometry irregularities and the fault slip distribution, we modeled a distributed fault slip model. To avoid gaps among the multiple fault planes when estimating the fault slip distribution, we generated a three-dimensional (3D) non-planar fault surface based on the geometry of the eight fault segments, and then a linear inversion approach was applied to estimate the slip parameter for each triangular dislocation element (see Methods). The optimized fault slip model fits the observations well (Supplementary Fig. S26). The distributed fault slip model shows heterogeneity, and a segmented pattern which appears to relate to the irregularities of the fault geometry. On the west side of the Huanghe step-over, the fault surface clearly dips toward the north (Fig. 4c). Correspondingly, the fault slip mainly distributes at a shallow depth and peaks at ~4 m, near to the ground surface (Fig. 4e). In contrast, the fault surface east of the Huanghe step-over shows subvertical dipping. The fault slip, however, goes deeper, with a wider extent, and peaks at ~5 m, around 3–6 km below the ground surface. Finally, the slip distribution on the southeast branch fault shows a smaller extent and peaks at ~2 m, around 2–6 km below the ground surface (Fig. 4f).

Discussion
While the irregularities of the fault dips of this event have previously been inferred from the locations of the aftershocks and geodetic near-field observations (Supplementary Table S1), our Bayesian approach explores all the possible fault geometries with eight scheduled fault segments.

The model reveals three main irregularities for the fault dip on the west and east sides of the epicenter and the southeast branch fault, respectively. On the west side of the epicenter, the model indicates north-dipping angles, which agree with the other geodetic estimates[21,23] and the model inferred from the aftershocks[16]. Nevertheless, the other results based on the aftershock tendency[14,15] indicate both north-dipping and south-dipping angles. This may have been caused by the lack of constraint of the high-resolution surface rupture traces because, compared with the surface rupture traces on the west side of the epicenter, the aftershock locations are mainly distributed on the north side (Fig. 1b). To the east side of the epicenter, our model, the other geodetic estimates[21,23], and the studies based on the aftershock tendency[14–16] all indicate dip angles greater than or equal to 80°, and therefore demonstrate a subvertical dipping fault geometry. Most notably, our estimate for the southeast branch is a south-dipping angle of 44 ± 5°. As shown in Supplementary Table S1, on the branch fault, our model is different from all the previous studies, and the closest result to our model is the estimate of a 64° south-dipping angle[24]. However, their result was based on a two-segment fault model obtained with a stepwise grid search that first determined the dip angle of the main segment and then fixed the geometry of the segment to determine the dip angle of the branch segment. In contrast, our model represents a globally optimized solution through simultaneously estimating the parameters of all the segments.

Our findings further illuminate the intricate nature of the southeastern branch fault. The double-segment model we employed for the southeastern branch reveals a dual characteristic of fault planes—nearly vertical and shallow-dipping, respectively. This distinct feature is mirrored in the aftershocks I and J within close proximity, which respectively display nearly vertical and shallow-dipping nodal planes. However, the complexity arising from varying segment lengths in the double-segment model introduces a challenge in determining the most appropriate fault lengths. This complexity, in turn, indirectly impacts the accurate estimation of fault dip angles. While the fault planes derived from the double-segment model do not precisely align with the spatial positions of aftershocks I and J, they do point to a potential scenario for the southeastern branch fault: it could manifest as either a vertical or shallow-dipping fault, or possibly a combination of both orientations.

In our investigation, we primarily leverage ground displacement data obtained through radar interferometry and pixel offset methods to constrain the fault parameters within the model. However, it's important to note that the pixel offset method does introduce a relatively high level of noise. Consequently, the estimation of fault parameters unavoidably becomes subject to the influence of data noise. Therefore, for a more comprehensive validation of our fault parameter estimation results, we anticipate the need for supplementary underground observational data in future studies.

If we consider the shallow-dipping strike-slip outcome of the southeastern branch to be highly probable, the forming of the shallow-dipping branch fault with the dominant strike-slip component may have been modulated by the strike direction of the Maduo-Gande fault (MGF) (Fig. 4c), and it highlights the complex stress environment that receives the shear loading across the fault system, but suffered from great compressional loading on the east section of the fault system during the 2021 Maduo earthquake. The compressional loading environment on the east section of the fault system can also be observed from the moderate to strong aftershock sequence (events A–N in Fig. 4c), in which four thrust faulting aftershocks (events A, C, J, and L) took place in the east section of the fault system, while the other aftershocks show a strike-slip mechanism across the entire fault system. This change of rupture directivities in the aftershocks from strike-slip motions to thrust components potentially implies a compressional seismogenic environment on the east section of the fault system. We also note that, on the east section of the fault system, the southeast branch fault (F8) is shallowly dipping, but the F7 fault segment is still subvertical (Fig. 4a). This implies that the compressional loading is mainly from the south side of the F7 fault segment.

The geological survey of the fault system of the Maduo earthquake shows the ~2-km-wide Huanghe step-over and the fault branching (Fig. 1b). These features are common in such settings, as large continental strike-slip earthquakes are often segmented[43]. Dynamic rupture models have previously demonstrated that fault step-over[44], bends[3], gaps[45], and splay[46] can either promote or inhibit rupture propagation. The inferred source kinematics of the 2021 Maduo earthquake indicate two possible rupture processes: one is rupture propagation with bilateral rupture speeds that are faster on the east side of the epicenter[22,47–49]; the other is rupture propagation with a stable rupture speed across the entire fault system[18,23]. Our estimates show obvious fault geometry complexity (segment F3 vs. segment F4, Fig. 4a) on both sides of the Huanghe step-over (~10 km west of the epicenter, Fig. 2a). It is indicated that fault segment F3 dips 75° to the north, whereas fault segment F4 dips 82° to the north, and the dip angle difference between the two segments is 7°. For the east section of the epicenter, the triple junction composed of

fault segments F6, F7, and F8 also shows geometrical complexity. The dip angle difference between fault segments F6 and F7 is 2°, which is smaller than the sum of their estimated uncertainties (±1° plus ± 2°, Fig. 3c). Nevertheless, fault segment F8 significantly differs from segments F6 and F7. The dip angle difference of segment F8 versus segments F6 and F7 exceeds ~45°. The larger the dip change along strike, the smaller the possibility for rupture propagation through a geometrical complexity[50]. Thus, the rupture process of the 2021 Maduo earthquake likely propagated from segments F4, F5, and F6 to segment F7, and segment F8 is likely active as an independent fault. The dip angle difference (5°, from F4 to F7) on the east side of the epicenter, compared to the dip angle variation (7°, from F4 to F1) on the west side of the epicenter, appears to support a stable rupture speed on the both sides of the epicenter.

Method

SAR data processing. We employed GMTSAR software[51] to process the SAR data. We used the 30-m resolution Shuttle Radar Topography Mission (SRTM) digital elevation map (DEM)[52] to remove the topographic signal, and the precise orbit information data were used to achieve the co-registration of the reference and secondary SAR images. In order to suppress the phase noise and improve the signal-to-noise ratio (SNR), we adopted a Gaussian filter with a 200-m wavelength to filter the interferograms, and the number of multi-looks in the range and azimuth directions was specified as 8:2[53]. All the interferograms were unwrapped using the statistical-cost network-flow algorithm for the phase unwrapping package[54]. We then geocoded the unwrapped interferograms with the WGS84 coordinate system. In addition, we also used the pixel offset tracking method to estimate the range offsets. Finally, we obtained four types of coseismic surface deformation datasets, i.e., two line-of-sight (LOS) displacement maps of Sentinel-1 interferograms on both the ascending and descending tracks (Fig. 2a, b) as well as two pixel offset maps of the Sentinel-1 ascending and descending orbits (Fig. 2c, d). These maps were downsampled with InSamp software[55] (Supplementary Figs. S1–S4), which simultaneously estimates variance-covariance matrices for the downsampled data points. The variance covariance matrices estimated by InSamp account for measurement uncertainties of downsampled data points in the inversion. Furthermore, to prevent spatial aliasing, we removed data points that are within 1 km of the fault trace.

Bayesian inference framework based on multiple geodetic datasets. We used eight segments along the surface rupture traces to interpret the fault system (Fig. 2a). We treated each fault segment as a plane with uniform slip. Although the uniform slip model does not characterize the detail of the fault slips, it avoids introducing the subjective component of a distributed slip model that needs to be regularized with a priori information (e.g., Laplacian smoothing), due to the inherent ill-posed problem in the inversion. In a uniform slip model, a fault plane is characterized by strike, dip, length (along strike), and width (along down-dip direction) parameters, and the corresponding strike-slip and dip-slip parameters. The strike angle and length of each fault segment are known (Fig. 2b), and thus for all eight fault segments, there are 16 geometrical parameters (dips and widths) and 16 slip parameters (strike slips and dip slips) to estimate.

We use θ and $\mathbf{m}$ to represent the fault geometry parameters and the vector of slip parameters, respectively. Here we have five datasets that are GNSS displacements ($\mathbf{D}_1$, Fig. 1b), and four SAR deformation maps ($\mathbf{D}_2$, $\mathbf{D}_3$, $\mathbf{D}_4$, and $\mathbf{D}_5$, Fig. 2). The five datasets denote the ground displacements corresponding to the underground faulting process (θ and $\mathbf{m}$) in the Earth's media. The i-th

observed dataset $\mathbf{D}_i$ of the stochastic model is given as:

$$\mathbf{D}_i = \mathbf{G}_i(\theta)\mathbf{m} + \mathbf{e}_i, i = 1, 2, 3, 4, 5 \quad (1)$$

where $\mathbf{D}_i$ is the M_i-dimensional vector of the i-th observed dataset; M_i is the number of data points of the i-th observed dataset; $\mathbf{G}_i(\theta)$ is the design matrix of the Green's function characterizing the ground displacements at locations of data points caused by the unit slip on all the fault planes in an elastic media[56]; $\mathbf{e}_i$ represents the vector of the observed errors for the i-th dataset.

In Bayes' theorem, the posterior probability density function (PDF) for parameters θ and $\mathbf{m}$ can be inferred from the observed data $\mathbf{D}$:

$$p(\theta, \mathbf{m}|D) \propto p(\mathbf{D}|\theta, \mathbf{m})p(\theta, \mathbf{m}) \quad (2)$$

where $p(\mathbf{D}|\theta, \mathbf{m})$ represents the PDF of the observed data $\mathbf{D}$ for given values of θ and $\mathbf{m}$, and $p(\theta, \mathbf{m})$ is the prior PDF of θ and $\mathbf{m}$. Therefore, $p(\mathbf{D}|\theta, \mathbf{m})$ and $p(\theta, \mathbf{m})$ jointly determine the posterior PDF of parameters θ and $\mathbf{m}$. Considering the independence among the five datasets $\{\mathbf{D}_1, \mathbf{D}_2, \cdots, \mathbf{D}_5\}$, $p(\mathbf{D}|\theta, \mathbf{m})$ can be written as:

$$p(\mathbf{D}|\theta, \mathbf{m}) = p(\mathbf{D}_1|\theta, \mathbf{m})p(\mathbf{D}_2|\theta, \mathbf{m})p(\mathbf{D}_N|\theta, \mathbf{m}) = \prod_{i=1}^{5} p(\mathbf{D}_i|\theta, \mathbf{m}) \quad (3)$$

Substituting Eq. (3) into Eq. (2) gives the posterior PDF of parameters θ and $\mathbf{m}$:

$$p(\theta, \mathbf{m}|D) \propto p(\theta, \mathbf{m}) \prod_{i=1}^{5} p(\mathbf{D}_i|\theta, \mathbf{m}) \quad (4)$$

To formulate $p(\mathbf{D}_i|\theta, \mathbf{m})$, it is assumed that the observed error $\mathbf{e}_i$ for the i-th dataset $\mathbf{D}_i$ follows a Gaussian distribution, i.e., $\mathbf{e}_i \sim N(\mathbf{0}, \sigma_i^2 \mathbf{C}_i)$. $\mathbf{C}_i$ denotes the covariance matrix for the i-th dataset and σ_i^2 is the hyperparameter to scale $\mathbf{C}_i$. Considering Eq. 1, the observed dataset $\mathbf{D}_i$ consequently follows a Gaussian distribution, i.e., $\mathbf{D}_i \sim N(\mathbf{G}_i(\theta)\mathbf{m}, \sigma_i^2 \mathbf{C}_i)$. Thus, $p(\mathbf{D}_i|\theta, \mathbf{m})$ can be analytically given as:

$$p(\mathbf{D}_i|\theta, \mathbf{m}, \sigma_i) = \left(2\pi\sigma_i^2\right)^{-M_j/2}|\mathbf{C}_i|^{-1/2}$$
$$\times \exp\left[-\frac{1}{2\sigma_i^2}\left(\mathbf{D}_i - \mathbf{G}_i(\theta)\mathbf{m}\right)^{\mathrm{T}}\mathbf{C}_i^{-1}\left(\mathbf{D}_i - \mathbf{G}_i(\theta)\mathbf{m}\right)\right] \quad (5)$$

The prior PDF $p(\theta, \mathbf{m}, \sigma_i)$ is conventionally set as a uniform distribution. Specifically, the dip angle of each fault plane is assigned to a uniform distribution between a north-dipping angle of 30° and a south-dipping angle of 30°, and the width of each fault plane is given as a uniform distribution between 0.1 km and 20 km. We impose a conventional nonnegative constraint on the strike-slip component of each fault plane and assign a uniform distribution between 0 m and 6 m. Nevertheless, there is no nonnegative constraint on the dip-slip component of each fault plane, and a uniform distribution between −4 m and 4 m for the dip-slip is set. Hyperparameter σ_i is treated as following a log-uniform distribution, $\log(\sigma_i^2) \sim U(-5, 5)$. We summarize the above settings in Supplementary Table S3. These settings form the prior PDF $p(\theta, \mathbf{m}, \sigma_i)$.

After formulating $p(\mathbf{D}_i, |, \theta, \mathbf{m}, \sigma_i)$ and the prior PDF $p(\theta, \mathbf{m}, \sigma_i)$, according to Eq. (4), the posterior PDF of the model parameters is given by:

$$p(\theta, \mathbf{m}, \sigma_i, |, \mathbf{D}) \propto p(\theta, \mathbf{m}, \sigma_i) \prod_{i=1}^{5} p(\mathbf{D}_i|\theta, \mathbf{m}, \sigma_i) \quad (6)$$

We applied the sequential Monte Carlo (SMC) method to

generate the samples of each member of the ensemble of Eq. (6). The SMC method samples the posterior PDF through a series of intermediate PDFs, in which a prior PDF is gradually developed into the target posterior PDF. The intermediate PDFs were determined by a tempering parameter γ_i:

$$p_i(\mathbf{x}|\boldsymbol{D}) \propto p(\mathbf{x})p(\mathbf{D}|\mathbf{x})^{\gamma_i}$$
$$i = 0, 1, \cdots, R \text{ and } 0 = \gamma_0 < \gamma_1 < \cdots < \gamma_R = 1 \qquad (7)$$

where $p(\mathbf{x}|\mathbf{D})$ is the posterior PDF for all the model parameters $\mathbf{x} = [\theta; \boldsymbol{m}; \sigma_1^2, , \sigma_5^2]$; $p(\mathbf{D}|\mathbf{x})$ is the likelihood function; $p(\mathbf{x})$ is the prior PDF; and R is the total sampling stages.

We utilized a Python code SMC sampler[57] to achieve the sampling process. We implemented the SMC sampler with parallel computing to generate numerous Markov chains, to improve the computational efficiency. To sample 1D marginal PDFs of all the model parameters from Eq. (6), we started the SMC algorithm with 1000 Markov chains, with each chain containing 400 steps. We initiated all the parameters with the distributions shown in Supplementary Table S3. The sampling procedure was carried out within 47 stages, and was optimized by the SMC sampler as it ran (Supplementary Fig. S5). The computing procedure took ~12000 CPU core hours. As our sampling of the Markov chains was made in parallel on a multi-node computing cluster of 1000 CPU cores, this resulted in ~12 h of computation time. Finally, 1000 posterior samples for each parameter were obtained. The sampling process for the dip angle, the width, the strike-slip, the dip-slip, and the hyperparameter is shown in Supplementary Figs. S6–S10. The 2D marginal PDFs between all the model parameters are shown in Supplementary Figs. S11–S15.

Distributed fault slip inversion. As fault segments F6 and F7 dip similarly ($85 \pm 1°$ vs. $86 \pm 2°$), we proposed constructing a non-planar fault surface that connects fault segments F1–F7, whereas fault segment F8 was built as a secondary fault surface. The top edge of the 3D fault surface can be constrained by the high-resolution surface rupture traces. The bottom edge of the primary fault (F1–F7) was set at the depth of 30 km, while the secondary fault (F8) is truncated at depth of 15 km, accounting for a small width and slip amplitude (Fig. 4a, b). Starting from the top edge, we followed the methodology of modeling non-planar fault geometry[32] and adjusted the bottom edge to match the dip angles of the eight fault segments by trial and error. We used 760 triangular dislocation elements to discretize the fault surface. To account for the decrease of data resolving power with depth, the sizes of the triangular dislocation elements were assigned to gradually increase with depth.

A linear inversion approach was applied to estimate the slip parameter for each triangular dislocation element. The conventional inversion approach for fault slip distribution with imposing a prior is to minimize an objective function, $||\mathbf{Gs} - \mathbf{D}||_2 + \beta^2||\mathbf{Ls}||_2$. The Green's function $\mathbf{G}$ can be calculated after fixing the source-receiver geometry. $\mathbf{s}$ is the vector of the slip parameters for all the triangular dislocation elements, and we assigned a strike-slip parameter and a dip-slip parameter for each triangular patch. The section $\beta^2||\mathbf{Ls}||_2$ is aimed at mitigating the ill-posed problem in the inversion. β^2 determines the strength of imposing a prior, $||\mathbf{Ls}||_2$. $\mathbf{L}$ is a matrix that describes the a priori knowledge imposed on the slip parameters, and here we treat $\mathbf{L}$ as a Laplacian operator[58] to regularize the slip distribution. The constrained linear least squares method[59] was used to solve the slip parameters, in which the strike-slip parameter was constrained to be nonnegative, accounting for the sinistral fault motions. The optimized fault slip model (Fig. 4e, f) was obtained based on an L-curve (Supplementary Fig. S24) and the estimated

uncertainties of fault slips are 0.2–0.6 m (Supplementary Fig. S25).

References

1. Fu, B. et al. Complex geometry and segmentation of the surface rupture associated with the 14 November 2001 great Kunlun earthquake, northern Tibet, China. *Tectonophysics.* **407**, 43–63 (2005).
2. Pulvirenti, F. et al. New fault slip distribution for the 2010 Mw 7.2 El Mayor Cucapah earthquake based on realistic 3D finite element inversions of coseismic displacements using space geodetic data. *J. Geophys. Res. Solid Earth.* **126**, e2020JB020016 (2021).
3. Lozos, J. C. et al. The effects of double fault bends on rupture propagation: a geometrical parameter study. *Bull. Seismol. Soc. Am.* **101**, 385–398 (2011).
4. Lavé, J. & Avouac, J. P. Active folding of fluvial terraces across the Siwaliks Hills, Himalayas of central Nepal. *J. Geophys. Res. Solid Earth.* **105**, 5735–5770 (2000).
5. Nábělek, J. et al. Underplating in the Himalaya-Tibet collision zone revealed by the Hi-CLIMB experiment. *Science* **325**, 1371–1374 (2009).
6. Shimizu, K. et al. Construction of fault geometry by finite-fault inversion of teleseismic data. *Geophys. J. Int.* **224**, 1003–1014 (2021).
7. Wang, X. & Zhan, Z. Seismotectonics and fault geometries of the 2019 ridgecrest sequence: insight from aftershock moment tensor catalog using 3-D green's functions. *J. Geophys. Res. Solid Earth.* **125**, e2020JB019577 (2020).
8. Riesner, M. et al. Building objective 3D fault representations in active tectonic settings. *Seismol. Res. Lett.* **88**, 831–839 (2017).
9. Avouac, J.-P. et al. The 2013, Mw 7.7 Balochistan earthquake, energetic strike-slip reactivation of a thrust fault. *Earth. Planet. Sci. Lett.* **391**, 128–134 (2014).
10. Elliott, J. R. et al. Himalayan megathrust geometry and relation to topography revealed by the Gorkha earthquake. *Nat. Geosci.* **9**, 174–180 (2016).
11. Wei, S. et al. Superficial simplicity of the 2010 El Mayor–Cucapah earthquake of Baja California in Mexico. *Nat. Geosci.* **4**, 615–618 (2011).
12. Liu, J. et al. Complete three-dimensional coseismic displacements due to the 2021 Maduo earthquake in Qinghai Province, China from Sentinel-1 and ALOS-2 SAR images. *Sci. China Earth Sci.* **65**, 687–697 (2022).
13. Ren, J. et al. Coseismic surface ruptures, slip distribution, and 3D seismogenic fault for the 2021 Mw 7.3 Maduo earthquake, central Tibetan Plateau, and its tectonic implications. *Tectonophysics.* **827**, 229275 (2022).
14. Wang, W. et al. Aftershock sequence relocation of the 2021 MS7.4 Maduo Earthquake, Qinghai, China. *Sci. China Earth Sci.* **64**, 1371–1380 (2021).
15. He, K. et al. Fault geometry and slip distribution of the 2021 Mw 7.4 Maduo, China, earthquake inferred from InSAR measurements and relocated aftershocks. *Seismol. Res. Lett.* **93**, 8–20 (2021).
16. Xu, Z. et al. Analysis of seismogenic structure of Madoi, Qinghai Ms7.4 earthquake on May 22, 2021. *Chinese J. Geophys.* **64**, 2657–2670 (2021).
17. Fang, J. et al. Earthquake cycle deformation associated with the 2021 Mw 7.4 Maduo (Eastern Tibet) earthquake: an intrablock rupture event on a slow-slipping fault from sentinel-1 InSAR and teleseismic data. *J. Geophys. Res. Solid Earth.* **127**, e2022JB024268 (2022).
18. Chen, K. et al. The 2021 Mw 7.4 Madoi earthquake: an archetype bilateral slip-pulse rupture arrested at a splay fault. *Geophys. Res. Lett.* **49**, e2021GL095243 (2022).
19. Jin, Z. & Fialko, Y. Coseismic and early postseismic deformation due to the 2021 M7.4 Maduo (China) earthquake. *Geophys. Res. Lett.* **48**, e2021GL095213 (2021).

20. Zhao, D. et al. Tectonic and geometric control on fault kinematics of the 2021 Mw7.3 Maduo (China) earthquake inferred from interseismic, coseismic, and postseismic InSAR observations. *Geophys. Res. Lett.* **48**, e2021GL095417 (2021).

21. He, L. et al. Coseismic and early postseismic slip models of the 2021 Mw 7.4 Maduo earthquake (Western China) estimated by space-based geodetic data. *Geophys. Res. Lett.* **48**, e2021GL095860 (2021).

22. Zhang, X. et al. Supershear rupture during the 2021Mw 7.4 Maduo, China, earthquake. *Geophys. Res. Lett.* **49**, e2022GL097984 (2022).

23. Wei, S. et al. Simultaneous rupture propagation through fault bifurcation of the 2021 Mw7.4 Maduo earthquake. *Geophys. Res. Lett.* **49**, e2022GL100283 (2022).

24. Hong, S. et al. Fault source model and stress changes of the 2021 Mw 7.4 Maduo earthquake, china, constrained by InSAR and GPS measurements. *Bull. Seismol. Soc. Am.* **112**, 1284–1296 (2022).

25. Fukuda, J. & Johnson, K. M. A fully bayesian inversion for spatial distribution of fault slip with objective smoothing. *Bull. Seismol. Soc. Am.* **98**, 1128–1146 (2008).

26. Ragon, T., Sladen, A. & Simons, M. Accounting for uncertain fault geometry in earthquake source inversions – I: theory and simplified application. *Geophys. J. Int.* **214**, 1174–1190 (2018).

27. Agata, R., Kasahara, A. & Yagi, Y. A Bayesian inference framework for fault slip distributions based on ensemble modelling of the uncertainty of underground structure: with a focus on uncertain fault dip. *Geophys. J. Int.* **225**, 1392–1411 (2021).

28. Gallovič, F. et al. Bayesian dynamic finite-fault inversion: 1. method and synthetic test. *J. Geophys. Res. Solid Earth.* **124**, 6949–6969 (2019).

29. Minson, S. E., Simons, M. & Beck, J. L. Bayesian inversion for finite fault earthquake source models I—theory and algorithm. *Geophys. J. Int.* **194**, 1701–1726 (2013).

30. Dal Zilio, L., Jolivet, R. & Dinther, Y. V. Segmentation of the main Himalayan thrust illuminated by bayesian inference of interseismic coupling. *Geophys. Res. Lett.* **47**, e2019GL086424 (2020).

31. Vasyura-Bathke, H. et al. The bayesian earthquake analysis tool. *Seismol. Res. Lett.* **91**, 1003–1018 (2020).

32. Dutta, R., Jónsson, S. & Vasyura-Bathke, H. Simultaneous bayesian estimation of non-planar fault geometry and spatially-variable slip. *J. Geophys. Res. Solid Earth.* **126**, e2020JB020441 (2021).

33. Wei, G., Chen, K. & Meng, H. Bayesian inversion of finite-fault earthquake slip model using geodetic data, solving for non-planar fault geometry, variable slip, and data weighting. *J. Geophys. Res. Solid Earth.* **128**, e2022JB025225 (2023).

34. Liu, C. et al. Coseismic deformation of the 2021 Mw7.4 Maduo earthquake from joint inversion of InSAR, GPS, and teleseismic data. *Earthq. Sci.* **34**, 436–446 (2021).

35. Bagnardi, M. & Hooper, A. Inversion of surface deformation data for rapid estimates of source parameters and uncertainties: a bayesian approach. *Geochem. Geophys. Geosyst.* **19**, 2194–2211 (2018).

36. Li, Z. et al. Coseismic deformation and slip distribution of 2021 Mw 7.4 Madoi earthquake from GNSS observation. *Geomat. Inf. Sci.* **46**, 1489–1497 (2021).

37. Zhao, L.-S. & Helmberger, D. V. Source estimation from broadband regional seismograms. *Bull. Seismol. Soc. Am.* **84**, 91–104 (1994).

38. Zhu, L. & Ben-Zion, Y. Parametrization of general seismic potency and moment tensors for source inversion of seismic waveform data. *Geophys. J. Int.* **194**, 839–843 (2013).

39. Zhu, L. & Rivera, L. A. A note on the dynamic and static displacements from a point source in multilayered media. *Geophys. J. Int.* **148**, 619–627 (2002).

40. Bai, Q. et al. gCAPjoint, a software package for full moment tensor inversion of moderately strong earthquakes with local and teleseismic waveforms. *Seismol. Res. Lett.* **91**, 3550–3562 (2020).

41. Jia, S.-X. et al. Investigation on diversity of crustal structures beneath the Bayan Har block. *Chin. J. Geophys.* **60**, 393–407 (2017).

42. Xin, H. et al. High-resolution lithospheric velocity structure of continental China by double-difference seismic travel-time tomography. *Seismol. Res. Lett.* **90**, 229–241 (2018).

43. Klinger, Y. Relation between continental strike-slip earthquake segmentation and thickness of the crust. *J. Geophys. Res.* **115**, B07306 (2010).

44. Yuan, J. & Zhu, S. Effects of stepover on rupture propagation. *Chin. J. Geophys.* **57**, 1510–1521 (2014).

45. Oglesby, D. D. What can surface-slip distributions tell us about fault connectivity at dept. *Bull. Seismol. Soc. Am.* **110**, 1025–1036 (2020).

46. Fliss, S. et al. Fault branching and rupture directivity. *J. Geophys. Res. Solid Earth.* **110**, B06312 (2005).

47. Yue, H. et al. Rupture process of the 2021 M7.4 Maduo earthquake and implication for deformation mode of the Songpan-Ganzi terrane in Tibetan Plateau. *Proc. Natl. Acad. Sci. USA* **119**, e2116445119 (2022).

48. Lyu, M. et al. Overall subshear but locally supershear rupture of the 2021 Mw 7.4 Maduo earthquake from high-rate GNSS waveforms and three-dimensional InSAR deformation. *Tectonophysics.* **839**, 229542 (2022).

49. Li, Q. et al. Source process featuring asymmetric rupture velocities of the 2021 Mw 7.4 Maduo, China, earthquake from teleseismic and geodetic data. *Seismol. Res. Lett.* **93**, 1429–1439 (2022).

50. Lozos, J. C. The effect of along-strike variation in dip on rupture propagation on strike-slip faults. *Geosphere.* **17**, 1616–1630 (2021).

51. Sandwell, D. et al. *GMTSAR: An InSAR Processing System Based on Generic Mapping Tools.* (Scripps Institution of Oceanography Technical Report, 2011).

52. Farr, T. G. et al. The shuttle radar topography mission. *Rev. Geophys.* **45**, RG2004 (2007).

53. Vaka, D. S., Rao, Y. S., & Singh, T. Surface deformation of the 2019 Mirpur Earthquake estimated from sentinel-1 insar data. In *2020 IEEE India Geoscience and Remote Sensing Symposium (InGARSS),* (IEEE, 2020).

54. Chen, C. W. & Zebker, H. A. Network approaches to two-dimensional phase unwrapping: intractability and two new algorithms. *J. Opt. Soc. Am. A Opt. Image Sci. Vis.* **17**, 401–414 (2000).

55. Lohman, R. B. & Barnhart, W. D. Evaluation of earthquake triggering during the 2005–2008 earthquake sequence on Qeshm Island, Iran. *J. Geophys. Res.* **115**, B12413 (2010).

56. Nikkhoo, M. & Walter, T. R. Triangular dislocation: an analytical, artefact-free solution. *Geophys. J. Int.* **201**, 1119–1141 (2015).

57. Dutta, R. Python codes for Sequential Monte Carlo sampling Technique (v1.0.0). *Zenodo* https://doi.org/10.5281/zenodo.3908931 (2020).

58. Maerten, F. et al. Inverting for slip on three-dimensional fault surfaces using angular dislocations. *Bull. Seismol. Soc. Am.* **95**, 1654–1665 (2005).

59. Coleman, T. F. & Li, Y. A reflective Newton method for minimizing a quadratic function subject to bounds on some of the variables. *SIAM J. Optim.* **6**, 1040–1058 (1996).

60. Zhang, G. et al. Boundaries between active-tectonic blocks and strong earthquakes in the China mainland. *Chinese J. Geophys.* **48**, 662–671 (2005).

61. Deng, Q. et al. Active tectonics and earthquake activities in China. *Earth Sci. Front.* **10**, 66–73 (2003).

Author contributions

G.W. and K.C. conceived and implemented the Bayesian inversion methodology, authoring the initial manuscript. M.L. processed the radar data, while W.G. conducted the point-source inversion process. Result analysis was carried out by L.D.Z. and L.Y., with H.T. providing the broadband seismic data. The paper underwent collective editing and extensive discussion involving all authors.

Competing interests

L.D.Z. is an Editorial Board Member for *Communications Earth & Environment*, but was not involved in the editorial review of, nor the decision to publish this article. All other authors declare no competing interest.

Additional information

Supplementary information The online version contains supplementary material available at https://doi.org/10.1038/s43247-023-00980-6.

Correspondence and requests for materials should be addressed to Kejie Chen.

Peer review information *Communications earth and environment* thanks the anonymous reviewers for their contribution to the peer review of this work. Primary Handling Editor: Joe Aslin. A peer review file is available.

Reprints and permission information is available at http://www.nature.com/reprints

Publisher's note Springer Nature remains neutral with regard to jurisdictional claims in published maps and institutional affiliations.